Determining Variability in Arctic Sea Ice Pressure Ridge Topography with ICESat-2

K. Duncan[1] and S. L. Farrell[2]

[1]Earth System Science Interdisciplinary Center, University of Maryland, College Park, MD, USA.

[2]Department Geographical Sciences, University of Maryland, College Park, MD, USA.

Corresponding author: Sinéad Louise Farrell (sineadf@umd.edu)

Farrell, Sinead Louise Orcid ID: 0000-0003-3222-2751

Duncan, Kyle Orcid ID: 0000-0001-6959-1206

For Submission to Geophysical Research Letters

Key Points

1. Advances in satellite laser altimetry techniques permit extensive mapping of pressure ridge topography across the Arctic Ocean
2. Our methods detect individual ridges and produce ice deformation statistics at resolutions previously only attainable with airborne lidar
3. As the oldest Arctic ice continues to decline, our results imply an on-going reduction in ridging intensity and hence form drag over time

Keywords

- 0750 Sea ice
- 0758 Remote sensing
- 0774 Dynamics
- 0770 Properties

Abstract

We investigate the characteristics and distribution of pressure ridges in Arctic sea ice using surface height profiles from the Advanced Topographic Laser Altimeter System (ATLAS) on ICESat-2. Applying a new algorithm to ATLAS measurements we derive the frequency and height of individual pressure ridges and map surface roughness and ridging intensity at the basin scale over three winters between 2019 and 2021. Comparisons with near-coincident airborne lidar data show that not only can we detect individual ridges 5.6 m wide, but also measure sail height more accurately than the existing ICESat-2 sea ice height product. We find regional variability in ridge morphology is large while annual variability is low. Ridge characteristics are not only related to their parent ice type but also their geographic location. High-resolution satellite altimetry data are valuable for characterizing sea ice deformation at short length-scales, providing observations that will advance ridge parameterizations in sea ice models.

Plain Language Summary

Pressure ridges, a result of convergence and deformation between ice floes, restrict the movement of air across sea ice and pose an impediment to transport across or through the ice by humans, animals or marine vessels. The laser altimeter on ICESat-2 provides height measurements of sea ice surface topography every 0.7 m in the direction of flight, from which we calculate surface roughness and measure the sail height and frequency of pressure ridges across the Arctic. We use coincident aircraft-mounted lidar data to evaluate the accuracy of ridge topography derived from ICESat-2. We show that our methods accurately distinguish ridges and reproduce sea ice deformation statistics at an along-track resolution previously only attainable from airborne platforms. We find that while year-to-year variability in pressure ridge morphology is low, regional variations are significant. In agreement with previous studies, we find distinct deformation characteristics depending on the parent ice type. The results demonstrate that high-resolution satellite altimeter observations can be used to derive detailed measurements of sea ice topography that will ultimately support process studies and advances in sea ice modeling.

1 Introduction

The advent of high-resolution satellite laser altimetry permits for the first time a complete mapping of sea ice surface topography at the basin scale. The Advanced Topographic Lidar

Altimeter System (ATLAS) on ICESat-2 has a footprint on Earth's surface approximately 11 m in diameter (Magruder et al., 2020), and a high pulse repetition frequency of 10 kHz, resulting in oversampled footprints at ~0.7 m along-track (Markus et al., 2017). This sampling configuration is ideal for mapping rough sea ice surface topography in high fidelity year round, allowing us to resolve individual ice floes, pressure ridges and leads at meter-scale (Farrell et al., 2020). This marks a significant advance in our capabilities for observing ice deformation compared to previous techniques, including airborne laser profiling (e.g., Hibler et al., 1974; Lowry and Wadhams, 1979; Wadhams et al., 1992; Dierking, 1995; Tan et al., 2012), upward looking and side scan sonar (e.g., Hibler et al., 1972; Davis and Wadhams, 1995), autonomous underwater vehicles (e.g., Wadhams and Doble, 2008), airborne electromagnetic induction techniques (Martin, 2007; Haas et al., 2009), and in situ observations (e.g., Timco and Burden, 1997; Strub-Klein and Sudom, 2012), that were each spatiotemporally limited. Leveraging widespread ICESat-2 observations, we extract the morphological characteristics of sea ice ridges across the Arctic Ocean and examine variations in ridging as a function of geographical area.

Pressure ridges that are formed through convergence increase ice thickness. They impact atmospheric flow across the ice surface and modify the momentum flux from the atmosphere through the ice to the ocean (Arya, 1973). Defined as a wall of broken ice forced up by pressure (WMO, 1970), ridges can be "fresh" (i.e., a first-year ridge) or "weathered and old". The sail, the portion above the local sea surface, consists of blocks of ice piled up and frozen together by contact, often with open voids. The submerged volume of broken ice, forced downwards by pressure, is termed an ice keel. Pressure ridges in isostatic equilibrium mature to roughly triangular sails with rounded crests (Parmerter and Coon, 1972). Early submarine observations revealed an uneven distribution of ridging across the Arctic with the heaviest deformation found north of Greenland and the Canadian Arctic Archipelago (e.g., Hibler et al., 1974; Bourke and McLaren, 1992).

Knowledge of sea ice topography is necessary to parameterize momentum transfer to the ocean in numerical simulations since surface stress increases with surface roughness (Martin et al., 2016; Tsamados et al., 2014). The roughness of the sea ice accumulates, and persists, throughout the growth season and, depending on the location of the ice, can potentially survive dissipation through melt or advection. Multiyear ice that has survived at least one summer melt season is hence rougher than first-year ice (Wadhams and Toberg, 2012). A form drag parameterization

based on direct observations of roughness (Tsamados et al., 2014) demonstrated both regional and temporal variability in form drag, and when implemented, resulted in a net decline in ice thickness, area and velocity compared to the model control run. Variability and trends in ice surface roughness due to the sustained multi-decadal loss of older ice (Perovich et al., 2019) are not adequately represented in sea ice models (Martin et al., 2016). Ridge metrics are also required for modeling the design load of sea ice on marine structures such as oil rigs and vessels (Timco and Burden, 1997) and the scattering of under-ice acoustics (Wadhams and Toberg, 2012).

Sea ice roughness is used here as a general term to describe all sources of ice deformation through ridging, rafting and rubbling, and includes hummocks as well as wind-driven undulations on the ice surface due to snowdrifts and sastrugi. Due to its dense along-track sampling, ICESat-2 has the capability to directly observe ice deformation at the scale of the individual pressure ridge. We can therefore retrieve ridge morphology. Here we calculate the standard deviation of surface elevation to estimate surface roughness (σ_h) and we characterize the upper expression of pressure ridges (sails) to obtain estimates of sail height (H_S) as well as ridge width (W_R), spacing (D_R) and intensity (I_R). We investigate regional variations at the end of winter (April) over three years between 2019 and 2021. Our derived statistics represent deformation accumulated throughout the winter period and hence include both fresh and weathered ridges. We analyze ridge morphology at different length scales, ranging from individual floes, to regional-scale deformation relevant for climate modelling, and upwards to the full basin scale, providing pan-Arctic metrics. Statistical models fit to the observations describe the characteristic shapes of the derived ridge dimensions in two regions with distinct ice deformation history. Our results are validated via comparison with near coincident Operation IceBridge (OIB) lidar data, collected during direct under-flights of ICESat-2 in April 2019.

2 Data and Methods

2.1 ATL03

Over sea ice, ATLAS (operating at 532 nm) obtains multibeam surface height profiles of the air/snow interface with respect to the reference ellipsoid (see e.g., Kwok et al., 2019b for further details). The ICESat-2 ATL03 global geolocated photon height data product (Neumann et al., 2021) is designed to be a single source for all photon data and ancillary information needed for

higher-level ICESat-2 data processing. ATL03 contains the latitude, longitude and height (h_{ph}) relative to the WGS-84 ellipsoid of all photons downlinked by the ATLAS instrument. The ATLAS pulse width of 1.5 ns results in photon height uncertainty of ~0.23 m (Kwok et al., 2019b).

2.2 ATL07

The ICESat-2 ATL07 sea ice height data product (Kwok et al., 2021) is derived from the ATL03 product. It contains sea ice and lead heights, adjusted for geoid and tidal variations and inverted barometer effects. It is calculated using 150-photon height aggregates in segments with variable lengths in the along-track direction ranging from ~27 m to 200 m and has a height precision of ~0.02 m over flat surfaces such as leads (Kwok et al., 2019b).

2.3 Ridge detection

The number of photons recorded by the ATLAS detector depends on both the morphology and reflectance of Earth's surface. Detections comprise photons scattered from the surface (signal) and background (noise) photons, including from solar background, detector noise and photons scattered by the atmosphere. The separation of background from surface photons is thus a critical step in the retrieval of accurate surface height profiles.

Kwok et al. (2019a) report that the ATL07 algorithm, which uses a fixed 150-photon aggregate designed for surface finding in the complex ice cover, does not capture the variability of the sea ice height distribution at short length-scales in areas of high surface roughness where pressure ridges are present. Since our goal is to retrieve pressure ridge topography, we must therefore apply a novel method that takes advantage of the full-resolution geolocated photon heights in the ATL03 product. The University of Maryland-Ridge Detection Algorithm (UMD-RDA) is designed to extract sea ice surface height, h, from ATL03 data. Over sea ice, ATL03 provides photon heights (h_{ph}) in a 30 m vertical window that includes the surface return. We construct a h_{ph} height distribution with a vertical bin size of 0.5 m and use a 5-shot horizontal aggregate (~2.8 m along-track distance). Photons clustered around the mode of the h_{ph} distribution are associated with the surface return and these are retained. If the h_{ph} distribution is bimodal, with modes in consecutive bins, the lowest mode is selected to indicate the surface mode (h_m). For bimodal h_{ph} distributions with modes that do not occur in consecutive bins, modal heights are compared with those of the previous shot and the mode closest to the previous modal height is

selected to indicate h_m. Only photons within the range (h_m + 10 m) ≥ h_{ph} ≥ (h_m – 2 m) are retained so as to adequately capture h_{ph} of ridge sails and leads, respectively. All other photons are considered background photons and are discarded. To reduce any remaining background photons from the final derivation of h, photons are further down selected, retaining only those within the 15^{th} – 85^{th} percentiles of the h_{ph} distribution. Sea ice surface height (h) is defined as the 99^{th} percentile of the remaining h_{ph} distribution and indicates the retrieval arising from the air/snow interface, i.e., the first surface interface encountered by the laser pulse.

The UMD-RDA surface finding approach is applied on a per-shot basis to retain h at a maximum along-track resolution of ~0.7 m. UMD-RDA height estimates are however only processed where ATL07 data are available (Kwok et al., 2021) and hence not produced for cloud-contaminated retrievals. Atmospheric, tide, and mean sea surface (MSS) geophysical height corrections are applied to h so as to obtain corrected heights (h_c) relative to the MSS. Here we use the Technical University of Denmark 2018 Mean Sea Surface (DTU18 MSS) model (Andersen et al., 2018). Ice surface roughness (σ_h) is estimated by taking the standard deviation of h_c in 25 km along-track segments for all cloud-free ICESat-2 sea ice data north of 65°N.

Next, the morphological characteristics of individual ridge sails on the ice surface are determined. The local level ice surface (H_L) is computed as the mode of the h_c height distribution in 25 km along-track segments. In segments with a large percentage of leads, the h_c distribution can be bimodal. In these cases, the highest modal elevation defines H_L. So as to extract ridge heights, all estimates of h_c are converted to height anomalies (h_a) relative to H_L. ICESat-2 has the capability to observe the surface topography of all floating morphological features of the ice cover that are larger than the minimum resolution, including ridges, rafts, rubble fields and hummocks as well as sastrugi and snowdrifts. Since our goal is to detect and characterize pressure ridges, we set an optimal cutoff height (H_0) above H_L, that defines the minimum ridge height (Lowry and Wadhams, 1979). Here, H_0 = 0.6 m (following Hibler et al., 1972; Duncan et al., 2018) and thus differentiates ridge sails from other surface features such as sastrugi. Independent ridges are defined using the Rayleigh criterion where the local maximum (peak) is at least twice as high as the neighboring minima (troughs) on both sides and the minima descend at least halfway toward H_L (Lowry and Wadhams, 1979; Tan et al., 2012). Independent ridges can therefore comprise multiple sails, and two adjacent topographical elements must fulfill the Rayleigh criterion to be resolved as separate ridge elements (Castellani et al., 2014). H_s is the maximum sail height of a

ridge relative to H_L (i.e., the maximum h_a within the ridge element). Following Timco and Burden (1997), ridge width (W_R) is measured as distance in the along-track direction between the points of intersection of H_L and the neighboring minima on either side of the ridge peak. Ridge spacing (D_R) is the peak-to-peak distance between consecutive H_S maxima. The latter two metrics will be impacted by the angle of intersection between the ICESat-2 orbit and the ridge orientation, but assuming heterogeneity in ice surface conditions across the Arctic, they should be robust at the basin scale.

2.4 Validation Data

ICESat-2's capabilities to measure sea ice surface topography in high resolution are quantified through comparisons of both the UMD-RDA and ATL07 sea ice heights with coincident aircraft observations. We use Airborne Topographic Mapper (ATM) lidar data (Studinger, 2020) collected during under-flights of ICESat-2 in April 2019 as part of NASA's OIB campaign (MacGregor et al., 2021). Analyzing these data, Kwok et al. (2019a) found that ATM and ATL07 surface height profiles were highly correlated when ATM data were averaged at the ATL07 segment length scale (~27 – 200 m) and manually coregistered. Larger differences were however found in areas of rough sea ice, when the ATL07 algorithm was unable to capture the full height distribution due to the segment-based approach (Kwok et al., 2019a).

Here we examine airborne observations from two underflights that had spatiotemporal coincidence with ICESat-2 orbits. On 19 April, 2019, ~142 km of coincident validation data were collected below ICESat-2 reference ground track (RGT) 325, while on 22 April, 2019 coincident data spanning ~233 km were collected below RGT 371. Since the ATM is a conically-scanning lidar (Krabill et al., 2002) it samples the ice surface unevenly (Duncan et al., 2018). We investigated the averaging length best suited for validation of the finer-scale ICESat-2 observations (Duncan et al., 2020), and here ATM data are extracted along the ICESat-2 height profiles using a n=5 nearest neighbor mean. UMD-RDA, ATL07 and ATM height profiles relative to the DTU18 MSS are sampled at 10 m along-track increments for direct comparison.

3 Kilometer-Scale Topography

First, we examine sea ice height at the floe scale O(1-10 km). We compare measurements of h_c derived from ATM, ATL07 and the UMD-RDA (Figure 1). The validation site (Figure 1c)

comprised the oldest, thickest sea ice in the Arctic (Perovich et al., 2019). The height variability of this heavily deformed surface (Figure 1a) is captured by all three methods. At the km-scale (Figure 1b) we can see both individual small ridges with a typical triangular shape in cross-section as well as the structure of ridge complexes, with multiple sails and irregular height profiles. Pressure ridge (H_s, W_R, D_R) and surface topography metrics (H_L and H_0) described in Section 2.3 are illustrated in Figure 1b.

Comparisons against ATM data show that the ATL07 algorithm acts as a low-pass filter, underestimating the height of individual ridge sails (red curves, Figures 1a, b), consistent with previous studies (Kwok et al., 2019a). Despite this, ATL07 heights are strongly correlated with ATM heights ($r \geq 0.82$, red dots, Figures 1d and e). They are however biased low by ~0.12 m, with median height underestimated by 0.06 – 0.08 m (Figures 1f and g). The largest differences are associated with rougher ice topography (Figures 1d-g).

UMD-RDA is designed to resolve individual ridges in the full-resolution photon data and the resulting height distributions are strongly correlated with ATM heights ($r \geq 0.86$, blue dots, Figures 1d and e). ATM and UMD-RDA mean, median and modal heights differ by $\leq$ 0.02 m (Figures 1f and g). Examining UMD-RDA heights across the central Arctic (ATL03 segment 04, Figure 1c), 3936 ridges are detected on RGT #325, and 5723 on RGT #371. The narrowest ridge resolved is 5.6 m wide. Modal ridge width is 35 m, and median and mean widths are ~71 m and ~90 m, respectively (Figure 1h and i).

4 Interannual Variability at Pan-Arctic Scales

To investigate the regional gradients in ice roughness and their interannual variability, σ_h in April 2019 – 2021 is mapped at 1/4° across the Arctic Ocean (Figure 2). The σ_h distribution histograms (insets, Figure 2) show little change in mean σ_h during the three-year period, which ranges 0.25-0.27 m. The maps however illustrate the dichotomy in σ_h between ice types, where the convergent ice regimes north of Greenland and Ellesmere Island result in the majority of multiyear ice with $\sigma_h \geq 0.3$ m, while first-year ice has $\sigma_h \leq 0.2$ m. Figure 2 also reveals advection of multiyear ice through the southern Beaufort Sea, which was particularly prevalent in April 2021 and the loss of multiyear ice through the Fram Strait.

Extending the analysis to the derived ridge metrics provides further insight into the state of the sea ice cover and the year-to-year variations in Arctic ice deformation. Here, H_{Smax} is the

maximum H_S per kilometer, while D_R is defined as the mean ridge spacing per 10 km. As with σ_h, these data are also mapped to a 1/4° grid. Regional variability in D_R does not directly map to H_{Smax} and hence a metric combining these variables is useful. Ridging intensity (I_R), first introduced by Hibler et al. (1974), is easily derived from laser profiling data and is defined as the mean sail height multiplied by the sail frequency per kilometer (i.e., $I_R = \langle H_S \rangle / \langle D_R \rangle$, where $\langle H_S \rangle$ is mean sail height and $\langle D_R \rangle$ is mean spacing). I_R is proportional to aerodynamic form drag of pressure ridges (Arya, 1973; Dierking, 1995). Figure 2 reveals that I_R is correlated with σ_h. Both metrics indicate higher than normal ridged ice along the Siberian coastline, particularly in the southwestern Chukchi Sea, East Siberian Sea and Laptev Sea. This localized ice deformation could be due to convergence against a land boundary or land-fast sea ice.

5 Regional-Scale Ice Deformation

Bridging between the kilometer and pan-Arctic scales (Figures 1 and 2) we analyze ICESat-2 data at the intermediate scale O(10 – 100 km), relevant to the typical resolution of climate models (Hunke et al., 2010). Pressure ridge distributions from two parts of the Arctic Ocean are compared: north of the Canadian Arctic Archipelago, region A encompasses older, rougher, thicker, mainly multi-year sea ice, while region B lies within the Beaufort Gyre encompassing younger, smoother, predominantly first-year ice. These two distinct regions were selected by examining the geographical distribution of σ_h between April 2019 and 2021 (Figure 2). Their areas are approximately equal so that the number of observations between the two regions is equivalent.

We calculate the distributions of σ_h, H_{Smax} and D_R in A and B and investigate the best statistical fits to these distributions. The regional results (Figure 3) show that all distributions have exponential tails denoting the fraction of pressure ridging present. Differences in ice deformation between the two regions are however apparent. In region A, average σ_h was ~0.4 m but decreased by 0.04 m over the three-year period (Figure 3a), while in region B, mean and modal σ_h remained approximately constant at ~0.2 m during the study period (Figure 3g). Surface height variability was larger in region A and the standard deviation of σ_h was approximately double that of region B (Figures 3a and g). The elongated tail of the H_{Smax} distribution in region A (Figure 3b) reveals that sails are frequently thicker than 3 m in older ice, but this is rare in younger ice (region B, Figure 3h). The data confirm that smaller ridges are more common across the ice cover than very

large, pressure ridge complexes (Figures 3b and h). Roberts et al. (2019) explained this theoretically, demonstrating that deformation of the ice cover seldom makes it to the later stages of ridging and that most sea ice is minimally crushed when the pack is compressed, since it is energetically preferable to form many small ridges rather than few large ridges. H_{Smax} in the older ice of region A averaged 0.63-0.72 m higher than in region B and modal H_{Smax} was approximately double that of region B (Figures 3b and h). 5% of sails in region A were ≥ 3.12 m, with 1 % of sails ≥ 4 m, while 95 % of all sails in region B were ≤ 2 m. Ridge sails were 2.6-2.8 times further apart in region B than in region A, with modal D_R of 375-475 m in region B compared to 125-225 m in region A (Figures 3c and i).

The non-Gaussian nature of the sea ice surface height distribution is demonstrated in Figures 3d and j, where σ_h observations are well fit by an exponential normal (exponentially modified Gaussian distribution) model in both regions, though the positively skewed surface topography is more evident in the older ice zone of region A. The statistical distribution of H_{Smax} in region A is best represented by a log-normal distribution (Figure 3e) and the tail is almost straight on the semi-log axis, indicating a negative exponential tail also commonly observed in ice thickness distributions (e.g., Haas et al., 2010). The H_{Smax} distribution in region B has not however acquired a fully negative exponential tail, and these data were also well represented by a Weibull distribution (not shown). Previous studies have shown D_R follows a log-normal distribution (e.g., Davis and Wadhams, 1995; Dierking, 1995). Our observations of D_R are best fit by a log-logistic distribution in regions A and B (Figures 3f and l) similar in shape to a log-normal distribution but with heavier tails. The results show a slight increase in D_R in both regions between April 2019 and 2021 suggesting less frequent ridging over time.

6 Discussion

ICESat-2 measurements of ice surface topography can reproduce sea ice deformation statistics at a resolution previously only attainable from aircraft surveys. Sea ice surface roughness (σ_h), sail height (H_{Smax}), ridge width (W_R), spacing (D_R) and intensity (I_R), measured at the end of winter between 2019 and 2021, yielded good coverage across a range of ice types and deformation regimes in the Arctic Ocean. Comparing the amount of topographic data assessed here with the published literature, we believe this is the largest ice deformation data set of its kind created to date (Duncan & Farrell, 2022). The ongoing availability of ICESat-2 data offers the possibility to

monitor σ_h year-round, map regional deformation events, derived from individual pressure ridges, soon after their occurrence, and track seasonal and interannual variability.

Building upon initial results presented in Farrell et al. (2020), we investigated ridge topography at a range of length scales O(1 – 1000 km). Consistent with previous studies (e.g., Hibler et al., 1974; Bourke and McLaren, 1992; Wadhams and Toberg, 2012) our results show that ice deformation is much more prevalent in multi-year ice zones than in seasonal areas. Our results also confirm that deformation varies not only with ice regime, but also with geographic location. Both H_{Smax} and I_R are greatest along the land boundaries of the multi-year ice zone and can be a factor of two larger than the deformation characteristics of multi-year ice at more northerly latitudes in the central Arctic. Localized deformation in the seasonal ice zone, due to convergence against a land boundary, can result in areas with I_R commensurate with that found in multi-year ice. H_{Smax} was well represented by a log-normal distribution in both rough and smooth ice regimes, but H_{Smax} was >60% larger in the roughest ice zone with little interannual variability across the three years studied. In the smoother ice zone, D_R was 2-3 times greater than in the rougher ice. H_{Smax} and I_R were lower overall in April 2021 than in 2019 and 2020, especially in the Eurasian Basin.

Although knowledge of pressure ridge characteristics such as H_S, D_R and I_R is necessary to model form drag, this information remains lacking in many Earth system models (Tsamados et al., 2014; Martin et al., 2016; Roberts et al., 2019). Martin et al. (2016) showed that such models lack a complete representation of feedbacks between ice roughness, thickness, drift and deformation, limiting the prediction of atmosphere-ice-ocean momentum transfer and how it varies with time. Roberts et al. (2019) suggest that pressure ridge observations are required to accurately model ice pack roughness and they propose that individual ridge statistics may be used to derive the evolution of the ice thickness distribution. ICESat-2 delivers observations of both individual pressure ridges at the scale of a model grid cell and σ_h and I_R at the basin scale thereby providing the needed ice deformation statistics to advance sea ice parameterizations.

First-year ice now comprises ~70% of the Arctic ice cover, compared to 35-50% in the 1980s (Perovich et al., 2019). As the Arctic rapidly transitions to a predominantly first-year ice cover with the continued loss of the oldest ice (Tschudi et al., 2020), ice topography will become dominated by the characteristics of pressure ridges in seasonal ice (Wadhams and Toberg, 2012). The sustained loss of multi-year ice, coupled with our basin-scale results, implies a decline in H_S,

an increase in D_R and an on-going reduction in I_R and hence form drag over time. Long-term and widespread observations of ice deformation from ICESat-2 will improve our understanding of how sea ice moderates the momentum flux between the atmosphere and ocean, providing a more complete picture of how and why the ice regime of the Arctic Ocean is transforming.

Data Availability Statement

NASA ICESat-2 ATL03 data are available at https://doi.org/10.5067/ATLAS/ATL03.005 and ATL07 sea ice height data are available at https://doi.org/10.5067/ATLAS/ATL07.005. NASA ATM data are available at https://doi.org/10.5067/19SIM5TXKPGT. The DTU18 MSS is available at https://ftp.space.dtu.dk/pub/DTU18/. Processed sea ice pressure ridge sail data described in this manuscript are available at https://doi.org/10.5281/zenodo.6772545.

Acknowledgements

This study is supported under NASA Cryosphere Program Grant 80NSSC20K0966 (ICESat-2 Science Team). The authors thank Jennifer Hutchings, Jacqueline Richter-Menge and Andrew Roberts for their useful discussions and thoughtful advice while we conceived and performed this study. We thank the ICESat-2 and IceBridge teams for processing the data used here.

Figures

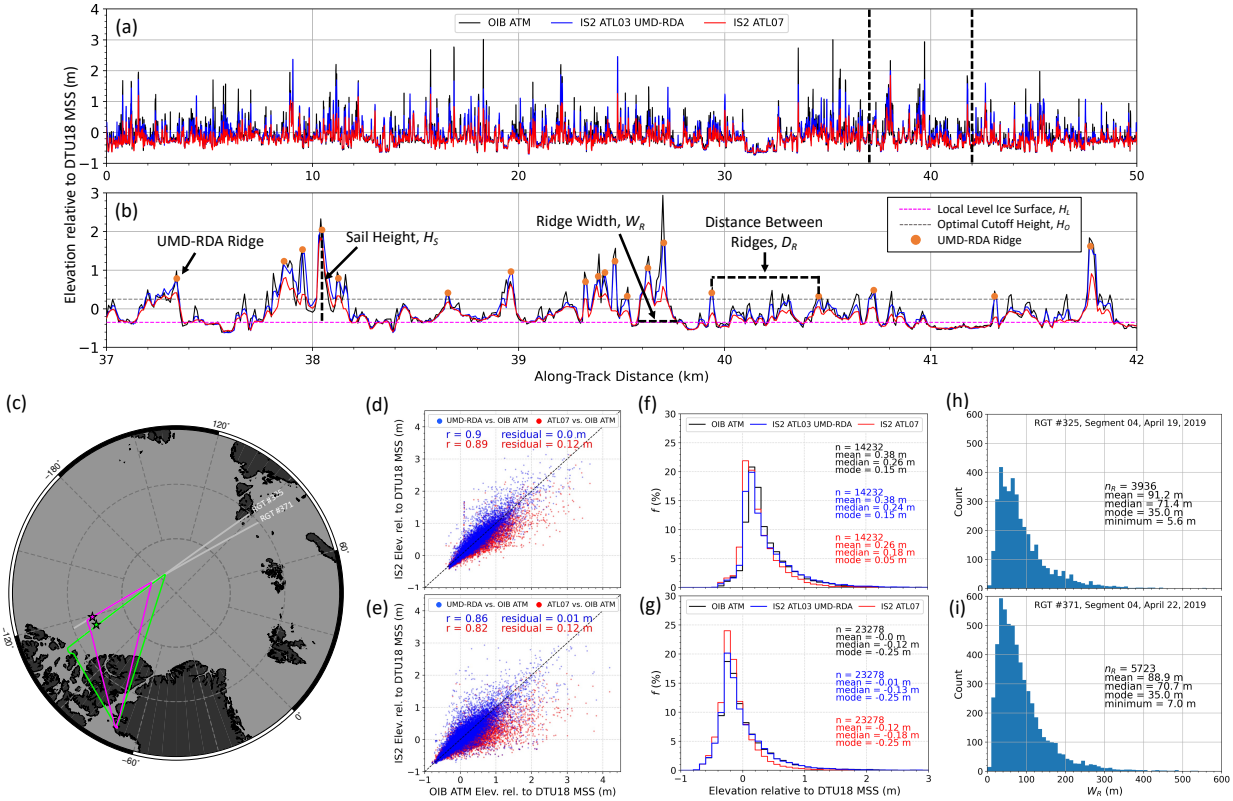

Figure 1. Arctic sea ice topography from ICESat-2. (a) OIB ATM airborne lidar (black), ICESat-2 ATL03 UMD-RDA (blue) and ATL07 (red) sea ice height profiles along a 50 km transect across multi-year sea ice (location indicated by magenta star in c) on 22 April, 2019. (b) A close-up 5-km view (section between vertical black dashed lines in a) illustrating surface topography and pressure ridge metrics defined in the text. (c) Map showing OIB flights on 19 (green) and 22 (magenta) April, 2019, with segment 04 of ICESat-2 reference ground tracks (RGTs) 325 and 371 (gray lines) and the locations of coincident validation data collection (stars). (d, e) Scatterplots comparing UMD-RDA (blue dots) and ATL07 (red dots) surface heights with coincident OIB ATM height measurements on 19 and 22 April, 2019, respectively. (f, g) Sea ice surface height distributions for coincident OIB ATM (black), UMD-RDA (blue), and ATL07 (red) data on 19 and 22 April, 2019, respectively. (h, i) Ridge width distributions derived from ALT03 segment 04 of RGTs 325 and 371, respectively, using the UMD-RDA.

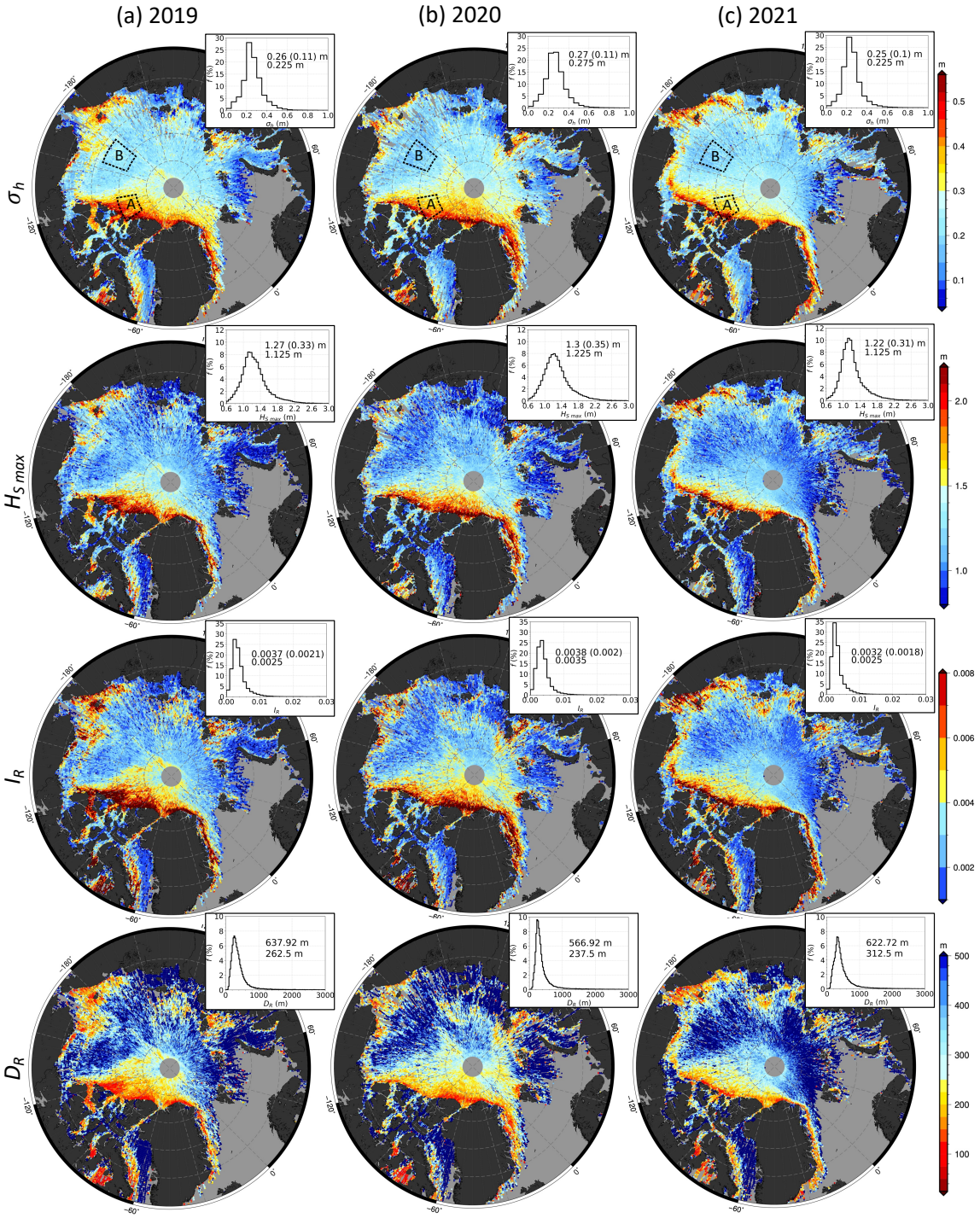

Figure 2. Pan-Arctic maps of surface roughness (σ_h), maximum sail height (H_{Smax}), ridge intensity (I_R), and distance between ridges (D_R) in April (a) 2019, (b) 2020 and (c) 2021. Insets show the histogram distributions with mean (standard deviation) and modal statistics provided to the right

of each histogram. Dashed black lines (top row) outline the locations (A, B) of the regional analysis described in the text.

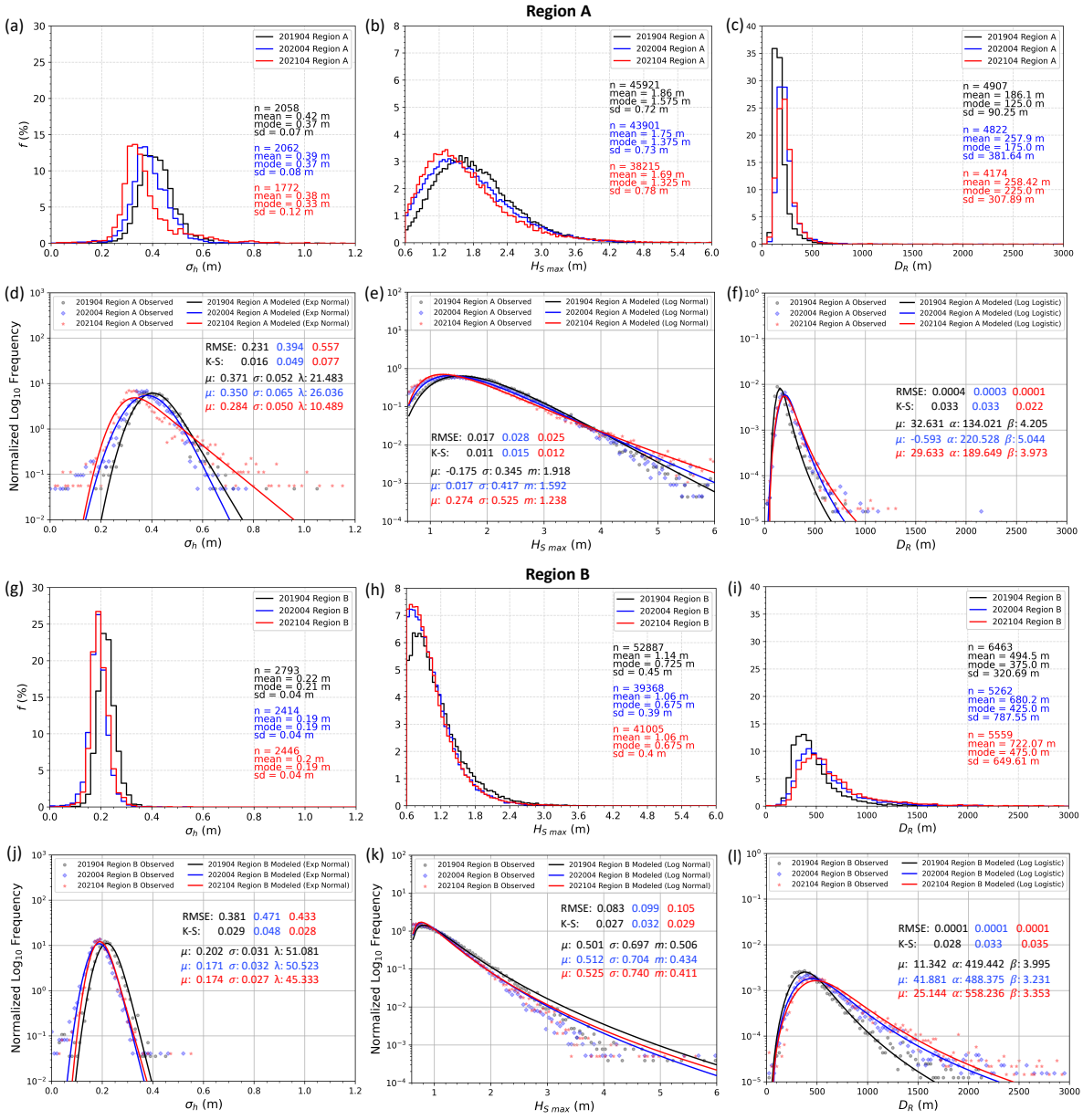

Figure 3. Statistical analysis of surface roughness (σ_h), maximum sail height (H_{Smax}) and distance between ridges (D_R) in April 2019 (black), 2020 (blue) and 2021 (red) for regions A (a – f) and B (g – l). Distributions of σ_h, H_{Smax} and D_R with the number of observations (n) and their mean, mode and standard deviation (sd) are shown on rows 1 and 3, for regions A and B, respectively. Semi-

log plots of σ_h, H_{Smax} and D_R and their model fits are on rows 2 and 4, for regions A and B, respectively. Root-mean-square error (RMSE), Kolmogorov–Smirnov (K-S) test statistics and the model parameters are shown to the right of each distribution.

References

Andersen, O. B., Rose, S. K., Knudsen, P. & Stenseng L. (2018). The DTU18 MSS Mean Sea Surface improvement from SAR altimetry. Technical University of Denmark, Copenhagen, Denmark.
https://ftp.space.dtu.dk/pub/DTU18/MSS_MATERIAL/PRESENTATIONS/DTU18MSS-V2.pdf

Arya, S. P. S. (1973). Contribution of form drag on pressure ridges to the air stress on Arctic ice. *J. Geophys. Res*., *78*(30), 7092–7099.

Bourke, R. H., and McLaren, A. S. (1992). Contour mapping of Arctic basin ice draft and roughness parameters. *J. Geophys. Res*., *97*(C11), 17715– 17728, doi:10.1029/92JC01857.

Castellani G., Lupkes, C., Hendricks, S., & Gerdes, R. (2014). Variability of Arctic sea ice topography and its impact on the atmospheric surface drag. *J. Geophys. Res. Oceans*, *119*, 6743–6762.

Davis, N. R., & Wadhams, P. (1995). A statistical analysis of Arctic pressure ridge morphology. *Journal of Geophysical Research*, *100*(C6), 10,915–10,925. https://doi.org/10.1029/95JC00007

Dierking, W. (1995). Laser profiling of the ice surface topography during the Winter Weddell Gyre Study 1992. *J. Geophys. Res.*, *100*(C3), 4807– 4820, doi:10.1029/94JC01938.

Duncan, K., & Farrell, S. L. (2020). High-Resolution Sea Ice Topography from ICESat-2. *Earth and Space Science Open Archive*, 1. https://doi.org/10.1002/essoar.10505000.1

Duncan, K. & Farrell, S. (2022). ICESat-2 Arctic Sea Ice Surface Topography from the University of Maryland-Ridge Detection Algorithm: April 2019, 2020, and 2021 (Version 1) [Data set]. Zenodo. https://doi.org/10.5281/zenodo.6772545

Duncan, K., Farrell, S. L., Connor, L. N., Richter-Menge, J., & Dominguez, R. (2018). High-resolution airborne observations of sea ice pressure-ridge sail height. *Annals of Glaciology*, *59*(76pt2), 137–147. https://doi.org/10.1017/aog.2018.2.

Duncan, K., Farrell, S. L., Hutchings, J., & Richter-Menge, J. (2020). Late Winter Observations of Sea Ice Pressure Ridge Sail Height. *IEEE Geoscience and Remote Sensing Letters.* https://doi.org/10.1109/LGRS.2020.3004724.

Farrell, S. L., Duncan, K., Buckley, E. M., Richter-Menge, J., & Li, R. (2020). Mapping Sea Ice Surface Topography in High Fidelity with ICESat-2. *Geophysical Research Letters*, *47*, e2020GL090708. https://doi.org /10.1029/2020GL090708.

Haas, C., Hendricks, S., Eicken, H., & Herber, A. (2010). Synoptic airborne thickness surveys reveal state of Arctic sea ice cover, *Geophys. Res. Lett*., *37*, L09501, doi:10.1029/2010GL042652.

Haas, C., Lobach, J., Hendricks, S., Rabenstein, L., & Pfaffling, A. (2009). Helicopter-borne measurements of sea ice thickness, using a small and lightweight, digital EM system. *Journal of Applied Geophysics*, *67*(3), 234-241.

Hibler III, W. D., Weeks, W. F., & Mock, S. J. (1972). Statistical aspects of sea-ice ridge distributions. *Journal of Geophysical Research*, *77*(30), 5954-5970.

Hibler, W.D., Mock, S.J. and Tucker, W.B. (1974). Classification and variation of sea ice ridging in the western Arctic basin. *J. Geophys. Res*., *79*(18), 2735–2743.

Hunke, E., Lipscomb, W., & Turner, A. (2010). Sea-ice models for climate study: Retrospective and new directions. *J. Glaciology*, *56*(200), 1162-1172. doi:10.3189/002214311796406095

Krabill, W. B., Abdalati, W., Frederick, E. B., Manizade, S. S., Martin, C. F., Sonntag, J. G., ... & Yungel, J. G. (2002). Aircraft laser altimetry measurement of elevation changes of the Greenland ice sheet: Technique and accuracy assessment. *J. Geodynamics*, *34*(3-4), 357-376.

Kwok, R., Kacimi, S., Markus, T., Kurtz, N. T., Studinger, M., Sonntag, J. G., et al. (2019a). ICESat-2 surface height and sea ice freeboard assessed with ATM lidar acquisitions from Operation IceBridge. *Geophysical Research Letters*, *46*, 11,228–11,236. https://doi.org/10.1029/2019GL084976.

Kwok, R., Markus, T., Kurtz, N. T., Petty, A. A., Neumann, T. A., Farrell, S. L., et al. (2019b). Surface height and sea ice freeboard of the Arctic Ocean from ICESat-2: Characteristics and early results. *Journal of Geophysical Research: Oceans, 124*(10), 6942-6959. https://doi.org/10.1029/2019JC015486.

Kwok, R., Petty, A., Cunningham, G., Markus, T., Hancock, D., Ivanoff, A., Wimert, J., Bagnardi, M., Kurtz, N., & the ICESat-2 Science Team. (2021). ATLAS/ICESat-2 L3A Sea Ice Height, Version 5. NASA Distributed Active Archive Center, National Snow and Ice Data Center, Boulder, Colorado USA. https://doi.org/10.5067/ATLAS/ATL07.005.

Lowry, R. T., and P. Wadhams (1979), On the statistical distribution of pressure ridges in sea ice. *J. Geophys. Res*., *84*(C5), 2487–2494, doi:10.1029/ JC084iC05p02487.

MacGregor, J. A., Boisvert, L. N., Medley, B., Petty, A. A., Harbeck, J. P., Bell, R. E., et al. (2021). The scientific legacy of NASA's Operation IceBridge. *Reviews of Geophysics*, 59, e2020RG000712. https://doi.org/10.1029/2020RG000712

Magruder, L.A., Brunt, K. M. & Alonzo, M. (2020). Early ICESat-2 on-orbit Geolocation Validation Using Ground- Based Corner Cube Retro-Reflectors. *Remote Sensing*, *12*(21), 3653. https://doi.org/10.3390/rs12213653.

Markus, T., Neumann, T., Martino, A., Abdalati, W., Brunt, K., Csatho, B., et al. (2017). The Ice, Cloud, and land Elevation Satellite-2 (ICESat-2): Science requirements, concept, and implementation. *Remote Sensing of Environment*, *190*, 260–273. https://doi.org/10.1016/j.rse.2016.12.029.

Martin, C. F., Krabill, W. B., Manizade, S., Russell, R., Sonntag, J. G., Swift, R. N., & Yungel, J. K. (2012). Airborne Topographic Mapper Calibration Procedures and Accuracy Assessment. NASA Technical Reports, *20120008479* (NASA/TM-2012-215891, GSFC.TM.5893.2012), http://hdl.handle.net/2060/20120008479, 32 pp., Natl. Aeronaut. and Space Admin., Washington, D. C.

Martin, T., Tsamados, M., Schroeder, D., & Feltham, D. (2016). The impact of variable sea ice roughness on changes in Arctic Ocean surface stress: A model study. *Journal of Geophysical Research: Oceans*, *121*, 1931–1952. https://doi.org/10.1002/2015JC011186.

Neumann, T. A., Brenner, A., Hancock, D., Robbins, J., Saba, J., Harbeck, K., Gibbons, A., Lee, J., Luthcke, S. B., Rebold, T., et al. (2021). ATLAS/ICESat-2 L2A Global Geolocated Photon Data, Version 5. NASA Distributed Active Archive Center, National Snow and Ice Data Center, Boulder, Colorado USA. https://doi.org/10.5067/ATLAS/ATL03.005.

Neumann, T. A., Martino, A. J., Markus, T., Bae, S., Bock, M. R., Brenner, A. C., ... & Thomas, T. C. (2019). The Ice, Cloud, and Land Elevation Satellite–2 Mission: A global geolocated photon product derived from the advanced topographic laser altimeter system. *Remote Sensing of Environment*, *233*, 111325. https://doi.org/10.1016/j.rse.2019.111325.

Parmerter, R. R., and Coon, M. D. (1972). Model of pressure ridge formation in sea ice. *J. Geophys. Res., 77*(33), 6565– 6575, doi:10.1029/JC077i033p06565.

Perovich, D., Meier, W., Tschudi, M., Farrell, S., Hendricks, S., Gerland, S., Kaleschke, L., Ricker, R., Tian-Kunze, X., Webster, M., & Wood, K. (2019). Sea Ice. Arctic Report Card 2019, J. Richter-Menge, M. L. Druckenmiller, and M. Jeffries, Eds., http://www.arctic.noaa.gov/Report-Card.

Roberts, A. F., Hunke, E. C., Kamal, S. M., Lipscomb, W. H., Horvat, C., & Maslowski, W. (2019). A variational method for sea ice ridging in Earth system models. *Journal of Advances in Modeling Earth Systems*, *11*, 771–805. https://doi.org/10.1029/2018MS001395.

Strub-Klein, L., & Sudom, D. (2012). A comprehensive analysis of the morphology of first-year sea ice ridges. *Cold Regions Science and Technology*, *82*, 94-109.

Studinger, M. (2013, updated 2020). *IceBridge ATM L1B elevation and return strength, Version 2 (ILATM1B)*. NASA Distributed Active Archive Center, National Snow and Ice Data Center, Boulder, Colorado, USA. https://doi.org/10.5067/19SIM5TXKPGT.

Tan, B., Li, Z., Lu, P., Haas, C. & Nicolaus, M. (2012). Morphology of sea ice pressure ridges in the northwestern Weddell Sea in winter. *J. Geophys. Res*., *117*, C06024, doi: 10.1029/2011JC007800.

Timco, G. W., & Burden, R. P. (1997). An analysis of the shapes of sea ice ridges. *Cold Regions Science and Technology*, *25*, 65–77. https://doi.org/10.1016/S0165-232X(96)00017-1

Tsamados M and 7 others (2014) Impact of atmospheric and oceanic form drag on simulations of Arctic sea ice. *J. Phys. Oceanog*., *44*, 1329–1353, doi: 10.1175/JPO-D-13-0215.1.

Tschudi, M. A., Meier, W. N., & Stewart, J. S. (2020). An enhancement to sea ice motion and age products at the National Snow and Ice Data Center (NSIDC). *The Cryosphere*, *14*(5), 1519-1536.

Wadhams, P., & Doble, M. J. (2008). Digital terrain mapping of the underside of sea ice from a small AUV. *Geophysical Research Letters*, *35*, L01501.https://doi.org/10.1029/2007GL031921

Wadhams, P., & Toberg, N. (2012). Changing characteristics of arctic pressure ridges. *Polar Science*, *6*(1), 71-77.

Wadhams, P., Tucker III, W. B., Krabill, W. B., Swift, R. N., Comiso, J. C., & Davis, N. R. (1992). Relationship between sea ice freeboard and draft in the Arctic Basin, and implications for ice thickness monitoring. *Journal of Geophysical Research: Oceans*, *97*(C12), 20325-20334.

World Meteorological Organization (1970). Sea ice nomenclature: Terminology, codes and illustrated glossary, WMO/OMM/BMO 259, TP145, World Meteorological Organization, Geneva. https://www.jcomm.info/components/com_oe/oe.php?task=download&id=27226&version=March 2014&lang=1&format=1.